Trace-element segregation to dislocation loops in experimentally heated zircon

EMILY M. PETERMAN^{1,*}, STEVEN M. REDDY^{2,3,†}, DAVID W. SAXEY^{3,}§, DENIS FOUGEROUSE^{2,3,‡}, M. ZAKARIA QUADIR^{4,#}, AND MICHAEL J. JERCINOVIC⁵

¹Department of Earth & Oceanographic Science, Bowdoin College, Brunswick, Maine 04011, U.S.A.

²School of Earth and Planetary Sciences, Curtin University, Perth, Western Australia 6845, Australia

³Geoscience Atom Probe, John de Laeter Centre, Curtin University, Perth, Western Australia 6102, Australia

⁴Microscopy and Microanalysis Facility, John de Laeter Centre, Curtin University, Perth, Western Australia 6102, Australia

⁵Department of Geosciences, University of Massachusetts, Amherst, Massachusetts 01003, U.S.A.

ABSTRACT

To evaluate the mechanisms driving nanoscale trace element mobility in radiation-damaged zircon, we analyzed two well-characterized Archean zircons from the Kaapvaal Craton (southern Africa): one zircon remained untreated and the other was experimentally heated in the laboratory at 1450 °C for 24 h. Atom probe tomography (APT) of the untreated zircon reveals homogeneously distributed trace elements. In contrast, APT of the experimentally heated zircon shows that Y, Mg, Al, and Pb+Yb segregate to a set of two morphologically and crystallographically distinct cluster populations that range from 5 nm tori to 25 nm toroidal polyhedra, which are confirmed to be dislocation loops by transmission electron microscopy (TEM). The dislocation loops lie in {100} and {001} planes; the edges are aligned with <100>, <101>, and <001>. The largest loops (up to 25 nm diameter) are located in {100} and characterized by high concentrations of Mg and Al, which are aligned with <001>. The 207 Pb/ 206 Pb measured from Pb atoms located within all of the loops $(0.264 \pm 0.025; 1\sigma)$ is consistent with present-day segregation and confirms that the dislocation loops formed during our experimental treatment. These experimentally induced loops are similar to clusters observed in zircon affected by natural geologic processes. We interpret that differences in cluster distribution, density, and composition between experimentally heated and geologically affected zircon are a function of the radiation dose, the pressure-temperature-time history, and the original composition of the zircon. These findings provide a framework for interpreting the significance of clustered trace elements and their isotopic characteristics in zircon. Our findings also suggest that the processes driving cluster formation in zircon can be replicated under laboratory conditions over human timescales, which may have practical implications for the mineralogical entrapment of significant nuclear elements.

Keywords: Zircon, radiation damage, APT, TEM, dislocation loop, annealing

Introduction

Zircon (ZrSiO₄) is commonly used across the geosciences to determine the timing and tempo of geologic events because it is chemically and physically robust, it incorporates U (and Th) during crystallization while excluding Pb, and trace element characteristics within the grain can be correlated with conditions of growth and recrystallization (e.g., Rubatto 2002; Hoskin and Schaltegger 2003). When subjected to changes in pressure (*P*), temperature (*T*), and/or fluids, zircon can anneal and/or recrystallize (Nasdala et al. 2001, 2002; Geisler 2002), which can potentially redistribute trace elements within the crystal (Rubatto 2002; Geisler et al. 2007; Harley et al. 2007).

One of the correlative factors associated with the mobility of trace elements in zircon is the accumulated radiation damage (Murakami et al. 1991; Meldrum et al. 1998; Cherniak and Watson 2003; Ewing et al. 2003). In recent years, quantitative analyses of zircon by atom probe tomography have revealed heterogeneous distributions of trace elements at the nanoscale. Examples include Pb+Y+Al diffusion to radiation-damaged sites (Valley et al. 2014, 2015), pipe diffusion of Pb along dislocation arrays into metamict domains within zircon (Piazolo et al. 2016), diffusive transport of trace elements to deformation microstructures (Piazolo et al. 2016; Reddy et al. 2016; Montalvo et al. 2019), and Pb+Y migration and entrapment within dislocation loops during prograde metamorphism (Peterman et al. 2016, 2019). These findings suggest that trace elements, including Pb, can be mobilized to discrete sites in radiation-damaged zircon, consistent with results from ion imaging (Kusiak et al. 2013; Ge et al. 2018). However, each of these studies were carried out on metamorphosed natural zircon specimens that record complex geologic and thermal histories. As a result, the details of the interpreted mechanisms of trace element mobility are difficult to unravel in these complex samples.

Here, we evaluate the relationships among radiation dam-

^{*} E-mail: epeterma@bowdoin.edu. Orcid 0000-0003-4902-2457

[†] Orcid 0000-0002-4726-5714

[‡] Orcid 0000-0003-3346-1121

[§] Orcid 0000-0001-7433-946X

[#] Orcid 0000-0003-1626-3748

age, recrystallization, and trace element mobility in zircon by integrating scanning electron microscopy (SEM), atom probe tomography (APT), and transmission electron microscopy (TEM) to analyze an experimentally heated Archean zircon with a well-characterized and simple thermal history. We compare our findings with results from an untreated zircon from the same sample. Our objectives are to evaluate if short duration, high-temperature (1450 °C for 24 h) heating produces new nanoscale defects and, if so, whether these features exhibit similar trace-element characteristics to those observed in natural zircon affected by geologic processes. Because the zircon originally crystallized in the Archean eon, sufficient quantities of U-derived radiogenic Pb isotopes should have accumulated, enabling the calculation of ²⁰⁷Pb/²⁰⁶Pb dates and the quantification of the timing of trace element migration. By comparing these nanoscale data sets, we aim to elucidate the primary drivers of trace element mobility and segregation in zircon, the crystallographic control on the distribution of these clusters, and the possible implications for the treatment of materials used for nuclear storage.

SAMPLE DESCRIPTION

This study examined euhedral zircon extracted from an Archean granitoid (sample SA16-24 from -26.045497, 31.428056; Baughman and Flowers 2020) within the southeastern Kaapvaal Craton, southern Africa. From the Archean through the Phanerozoic eons, the Kaapvaal Craton was involved

in a series of terrane accretions and orogenic events, including the Namaqua-Natal orogenesis, the assembly of Rodinia, and the assembly and breakup of Pangea (e.g., de Wit et al. 1992; Baughman and Flowers 2020). The Kaapvaal Craton was initially stabilized in the Archean eon (3.6 to 3.0 Ga) and cooled to <300 °C by 2.7 Ga, as constrained by U-Pb titanite and apatite geochronology (Schoene and Bowring 2007) and 40 Ar/39 Ar biotite thermochronology (Layer et al. 1992). The crystallization age of the studied granitoid has been best constrained by analyses of 15 air-abraded zircon grains from a nearby granitoid of the same gneiss complex, which yields a mean age of 3.13 ± 0.06 Ga (1σ) (AGC01-4; Schoene and Bowring 2007). The post-crystallization thermal history of the studied granitoid as constrained by (U-Th)/He zircon analysis includes a low-temperature event $(150-250 \,^{\circ}\text{C})$ between 1.2 and 1.0 Ga and burial at up to 160 $^{\circ}\text{C}$ ca. 200 Ma ago (Baughman and Flowers 2020).

METHODS

Five euhedral zircon grains ~350 \times 150 μm were air-annealed in a covered Pt crucible at 1450 °C for 24 h in a Deltech furnace at Stanford University. The temperature was increased at 400 °C/h until reaching the 1450 °C set point. A representative grain from this aliquot was selected for APT analysis and mounted in a 1" (2.54 cm) epoxy round along with representative zircon grains that were untreated. The mount was progressively polished to expose the interior. Following a 1 μ m polishing step, the mount was affixed to a halved brass rod and polished with colloidal silica for 3 h on a Buehler VibroMet2 vibratory polisher. The mount was thoroughly rinsed with water and ethanol and dried in a desiccator overnight. A 10 nm carbon coat was evaporated onto the mount to minimize charging during imaging. Secondary electron and cathodoluminescence (CL) images (Fig. 1) were collected on the Tescan Vega3 SEM at Bowdoin College operated at 14 kV, 0.3 to 1 nA. Post-APT and post-TEM CL images were acquired on the Tescan CLARA field emission SEM at Curtin University using a 10 kV, 300 pA beam.

Crystallographic orientations were measured using an Oxford Instruments NordlysMax³ electron backscatter diffraction (EBSD) system attached to the Tescan Vega3 SEM at Bowdoin College. The SEM was operated at 20 kV, 10 nA at a working distance of 25 mm, with the mount tilted 70° toward the EBSD detector.

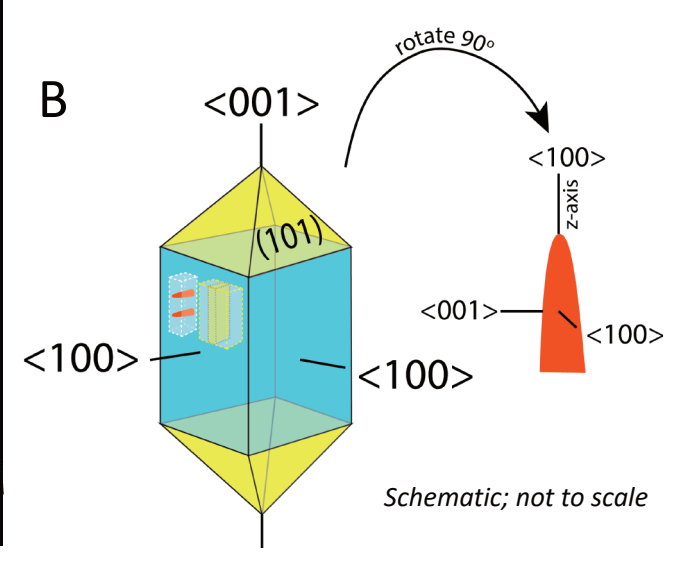


FIGURE 1. (a) Cathodoluminescence (CL) image of the analyzed zircon. Yellow box marks location of TEM foil; white box marks lift out location for atom probe specimens. Cyan dots mark the EPMA transect; box outlines the points used to determine U and Th concentrations. Pole figure shows the <100> and <001> of this grain, as measured by EBSD. (b) Schematic diagram of zircon with relevant crystallographic axes and planes marked; APT specimens (orange) and TEM foil (yellow) shown in their crystallographic context. (Color online.)

EBSD data were acquired with Oxford Instruments AZtec 3.4 software. Acquisition settings were 4×4 binning, gain = 7, Hough resolution = 60, 7 bands. Lattice parameters for the zircon match unit were from Hazen and Finger (1979); the measured mean angular deviations (MAD) for the seven indexed bands were <1°. Data were post-processed with Oxford Instruments Channel 5.12 software suite to remove non-systematic misindexed points (wild spikes), and a 6 nearest-neighbors routine was used to interpolate unindexed pixels.

Atom probe and TEM specimens were prepared at Curtin University using a Tescan Lyra3 Ga+ focused ion beam SEM (FIB-SEM) at Curtin University. APT specimens were mounted onto prefabricated Si posts on a specimen coupon and progressively sharpened by a Ga+ ion beam using an annular milling routine. The TEM specimen was mounted on a Cu grid and thinned to $\sim\!50$ nm. For both APT and TEM specimens, the final stage of sample preparation involved a low-voltage (2 kV) step to remove Ga implantation artifacts. Additional details of the specimen preparation technique are provided in Rickard et al. (2020).

Atom probe specimens were analyzed using laser-assisted APT on the Cameca LEAP 4000X HR at the Geoscience Atom Probe Facility at Curtin University. The atom probe was operated with a laser pulse energy of 300 pJ, at a frequency of 200 kHz. Field evaporation was controlled by maintaining a constant detection rate as voltage was steadily increased throughout the analysis. Reconstructions of the time-of-flight data were undertaken using a voltage evolution model and an assumed evaporation field of 32 V/nm (Saxey et al. 2019). The full acquisition and reconstruction parameters are given in Online Materials¹ Table OM1, following Blum et al. (2018), and a representative mass spectrum is included as Online Materials1 Fig. OM1. Run conditions and our procedure for calculating and applying background corrections to the 207Pb/206Pb ratio are also provided in the Online Materials¹. Details of the APT methodology are described in Reddy et al. (2020). To evaluate the trace element concentrations within nanoscale features, we used Cameca's IVAS 3.8.4 software to construct proximity histograms (proxigrams; Hellman et al. 2000). Proxigrams are aggregated 1D radial histograms and were calculated using a designated isoconcentration surface (0.03 at% Mg) and are measured from this surface into the nanoscale features within each specimen.

TEM analyses were performed on the experimentally heated zircon using Curtin University's FEI Talos FS200X FEG TEM operated at 200 kV and equipped with a Super-X EDS detector. A double tilt holder was used to tilt the sample toward the intended crystallographic zone axis. The orientation was determined by navigating through the convergent beam electron diffraction generated Kikuchi patterns and measuring the lattice spacing.

U and Th concentrations were measured along a transect (Fig. 1a) by electron probe microanalysis (EPMA) on the Cameca UltraChron at the University of Massachusetts-Amherst. Analyses were done at 20 kV, 400 nA with a focused beam. Th and U were analyzed using the ThM α and UM β emission lines using large PET (LPET) and very large PET (VLPET) monochromators, integrating counts from two spectrometers for each element, using a count time of 730 s each. Background estimation was done through multipoint acquisition for ThM α and UM β (Allaz et al. 2019) and exponential regression; interference corrections for ThM γ and HoL α_2 on the UM β emission line were applied. Matrix corrections were implemented via the PAP method (Pouchou and Pichoir 1984) and included a stoichiometric zircon composition along with measured values of Y, Hf, and heavy rare earth elements. Analysis was performed using Cameca's Peaksight interface for hardware setup (beam tuning, imaging for analysis positioning), and quantitative analysis was done using Probe for EPMA software (Probe Software, Inc.).

RESULTS

Prior to annealing, portions of some zircon grains were rusty red. After annealing, rusty red domains changed color to cloudy white, and transparent domains remained transparent.

SEM-CL

The center of the experimentally heated zircon grain features complexly zoned domains that are surrounded by a mottled texture (Fig. 1). The zircon surrounding these smaller domains is characterized by fine-scale zoning; this domain is truncated by zircon that has higher contrast, fine-scale CL zoning. These internal textures are all consistent with igneous processes. The grain has a network of intersecting healed fractures that are dark in CL and several through-going fractures. The APT

specimens and TEM foil were prepared from the domain showing fine-scale zoning. The untreated zircon (Online Materials¹ Fig. OM2) contains an inclusion-rich core with oscillatory zoning patterns consistent with igneous growth. This grain also has a network of intersecting healed fractures that are dark in CL and several intersecting, through-going fractures. The APT specimen was prepared from the zircon core (see Online Materials¹ Fig. OM3).

SEM-EBSD

Crystallographic orientation data, as measured by EBSD, confirms that <001> and one of the <100> axes are along the plane of the polished surface for both analyzed zircons. The <001> direction is oriented parallel to the long axis of the zircon; <100> axes are perpendicular to <001>, with one <100> direction oriented perpendicular to the sample surface (inset, Fig. 1a). Neither zircon exhibit evidence of misorientation associated with crystal plasticity (Online Materials¹ Fig. OM2) (Reddy et al. 2007). The APT specimens were prepared perpendicular to the polished surface (Fig. 1b) such that the z-axis of each atom probe specimen corresponds to the <100> axis normal to the polished surface and parallel to the crystallographic {100}, as shown schematically in Figure 1b.

Atom probe tomography (APT)

Experimentally treated zircon. Anomalously high concentrations of trace elements are found in clusters distributed throughout the two atom probe specimens measured from the experimentally treated zircon (Fig. 2). The clusters can be classified into two categories based upon size, crystallographic orientation, and composition. An isoconcentration surface of 0.03 at% Mg was used to define the spatial extent of both sets of clusters; the proxigrams show radial profiles of trace elements concentrations from the isoconcentration surface into the clusters. Large clusters with a toroidal polyhedral morphology (\sim 10–25 nm diameter, 10 nm thick) are parallel to {100}, with the toroidal axis oriented parallel to one of the <100> directions (Fig. 2c). These large clusters yield high concentrations of Y, Mg, and Al (Fig. 3). Within the clusters, Y exceeds 6.2 at%; Mg and Al are \sim 2 at% and preferentially aligned with <001>. Yb and Pb are above background (up to 0.5 and 0.17 at%), but concentrations of Ca, P, U, and Hf are not elevated within the clusters. For comparison, trace element concentrations (in at%, 1σ) in the matrix are as follows: $Y = 0.218 \pm 0.009$, $Mg = 0.006 \pm 0.001$, $A1 = 0.022 \pm 0.003$, $Yb = 0.019 \pm 0.001$, and $Pb \sim 0.004 \pm 0.001$.

Smaller, similarly shaped clusters (~5–15 nm diameter) are oriented parallel to {100} and {001}; these clusters are characterized by high concentrations of Y, Mg, and Al (Figs. 2d and 3). Clusters with the toroidal axis oriented parallel to the z-axis of the specimen can be difficult to recognize as torus-shaped features, which may be related to an evaporation effect wherein the geochemical difference between the clusters and the specimen matrix leads to a local field effect and ion trajectory aberrations (e.g., Fougerouse et al. 2016; Peterman et al. 2016). Y concentrations are as high as 7 at%, whereas Mg and Al reach 1.5 at%. Similar to the larger clusters, Yb and Pb are above background (up to 0.5 at%), but Ca, P, U, and Hf are not elevated within the clusters.

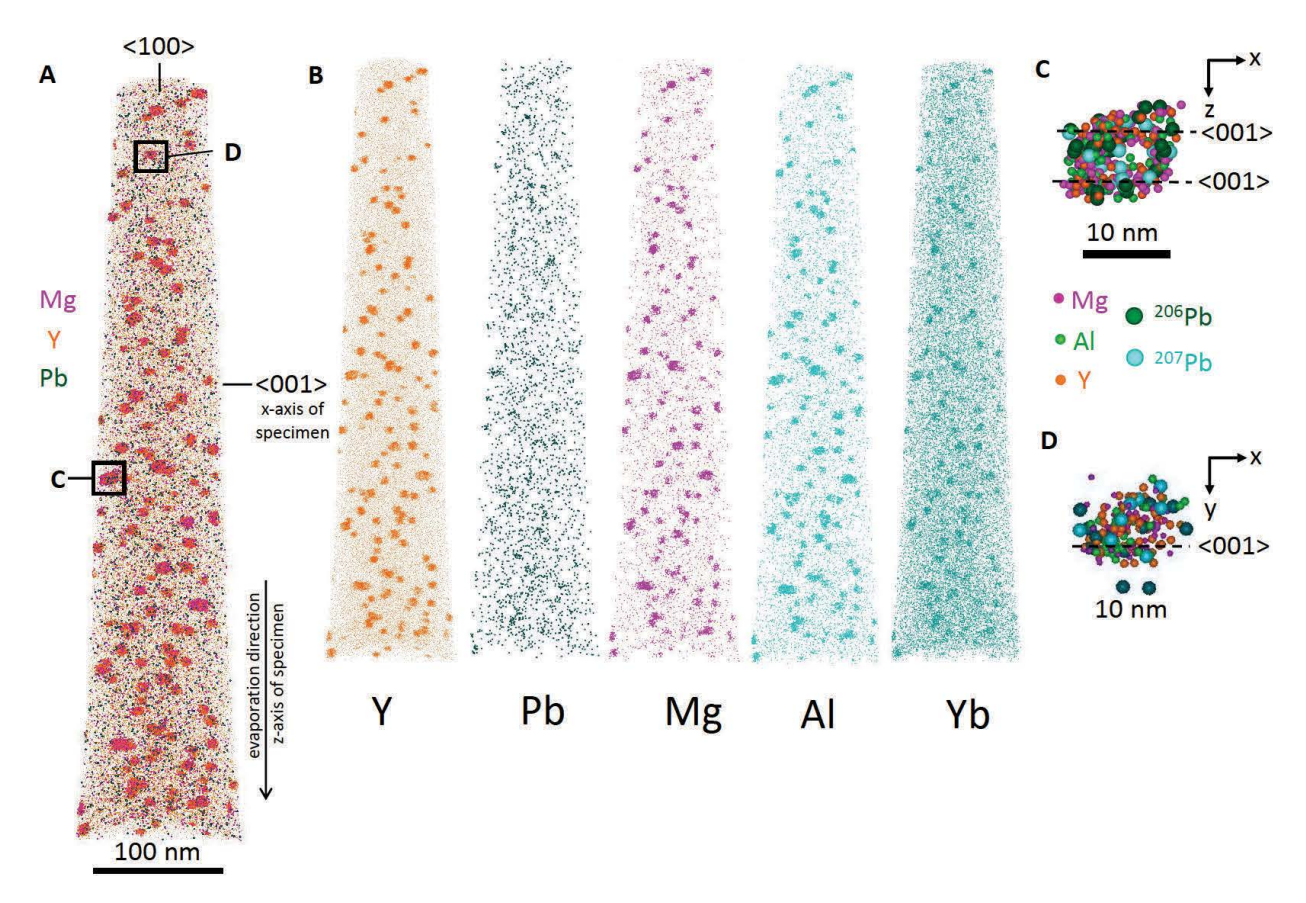


FIGURE 2. Atom probe tomography reconstructions from the experimentally heated zircon. Each point represents an atom; colors reflect different elements. (a) Whole specimen, multiple elements. (b) Single element reconstructions. (c and d) Close-up images of representative clusters; c is in the x-z plane of the specimen; d is in the x-y plane of the specimen. (Color online.)

The background-corrected $^{207}\text{Pb}/^{206}\text{Pb}$ calculated from within the clusters is 0.264 ± 0.025 (1σ), with no significant difference observed between the large and small clusters (0.302 ± 0.067 and 0.255 ± 0.027 , respectively; both 1σ). Assuming concordance, no initial common Pb, and accepted decay constants (Schoene

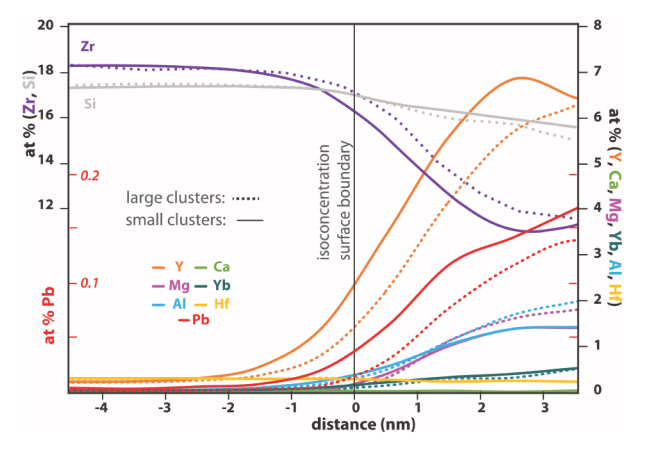


FIGURE 3. Proxigram shows changes in concentration (at%) with respect to the edge of the cluster in nm. Clusters were defined by an isoconcentration surface of 0.03 at% Mg. (Color online.)

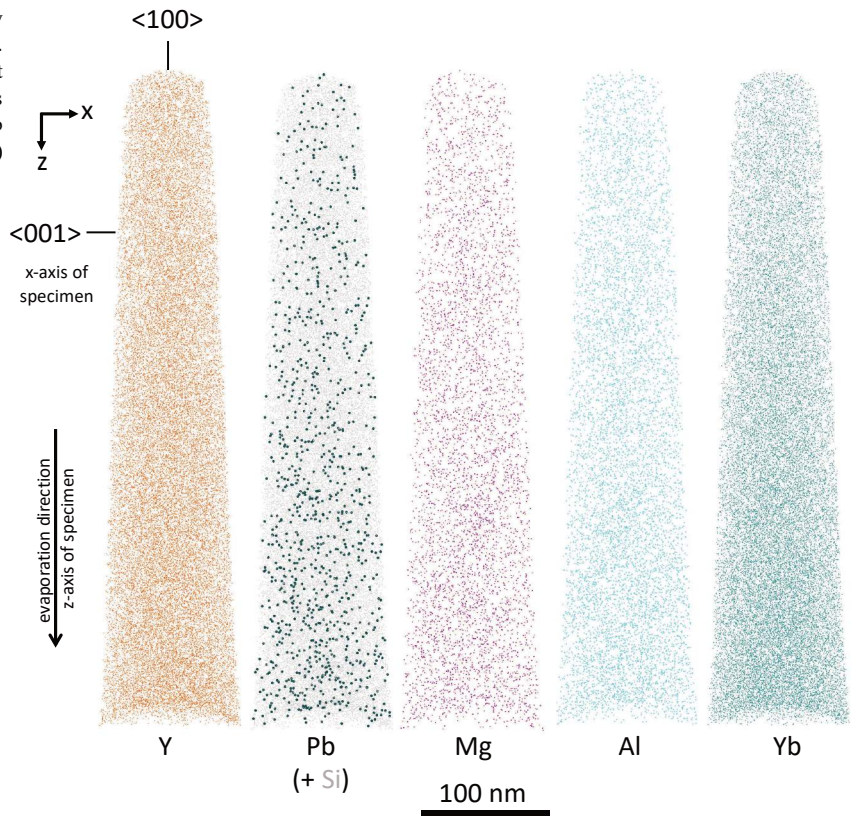
2014), the calculated ratio corresponds to a crystallization age of 3268 \pm 150 Ma (1 $\!\sigma$).

Untreated zircon. Atom probe reconstructions of a specimen prepared from the untreated zircon show that all trace elements are distributed homogeneously—there is no evidence of any trace element clustering (Fig. 4).

Transmission electron microscopy (TEM)

Bright-field TEM images (Fig. 5) show heterogeneously distributed, lens-shaped features, many of which exhibit multiple sets of Moiré fringes that are the product of the superposition of the matrix lattice over the lattice within the lens-shaped feature. The size, density, and morphology of these features compare favorably with the clusters observed via APT. These features can be subdivided into two dominant size distributions: 10-25 and 5-15 nm. The edges of these features are aligned with the <100> and <001> (Figs. 5a and 5b); some edges are also aligned with <101> (Fig. 5c). Close inspection shows that the rounded edge segments are defined by steps across the lattice along the {100}, {001}, and {101} planes, indicating that the features are crystallographically constrained and best described as having a toroidal polyhedral morphology. Compositional analysis by STEM-EDS indicates high concentrations of Al and Mg (Figs. 5d and 5e) within the dislocation loops; Y concentrations are also high and Pb is below detection (0.2 at%).

► FIGURE 4. Atom probe tomography reconstructions from the untreated zircon. Each point represents an atom; colors reflect different elements. Crystallographic directions and specimen orientations as marked. Pb (green) is shown with Si (gray). (Color online.)



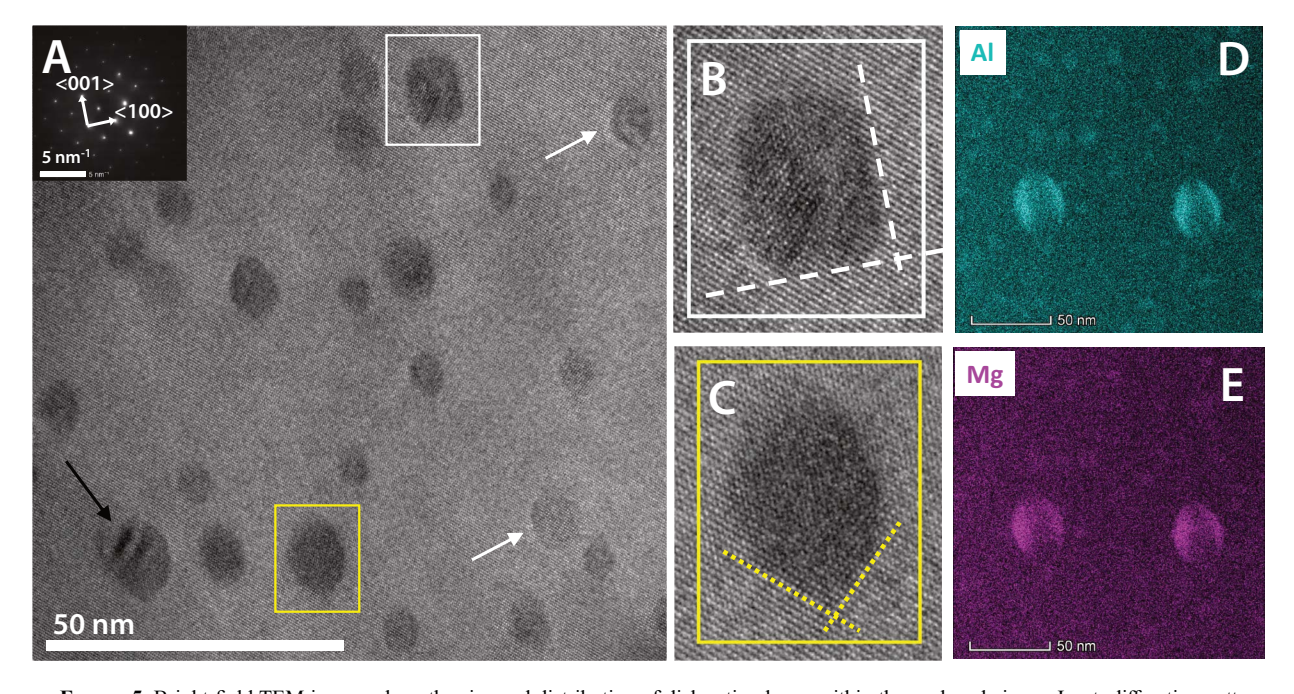


FIGURE 5. Bright-field TEM images show the size and distribution of dislocation loops within the analyzed zircon. Inset: diffraction pattern with <001> and <100> identified; all images were collected in the same orientation. (a) White arrows mark strained regions of the lattice; black arrow indicates Moiré fringes. The edges of the loop in **b** are aligned with <100> and <001>; these planes are shown by white dashed lines. The edges of the loop in **c** are aligned with <101> (shown by yellow dotted lines), <100> and <001>. Compositional maps acquired via STEM-EDS of Al (d) and Mg (e) within dislocation loops; maps were collected from an area adjacent to the region shown in a. (Color online.)

EPMA

Across the region of interest in the experimentally heated grain, U concentrations range from 177 to 346 ppm and Th concentrations from 99 to 255 ppm. Individual spot analyses have measurement uncertainties of ~4%. Because we cannot directly correlate the U and Th concentrations with the atom probe specimens, we used the mean concentrations for U and Th (249 ± 43 and 163 ± 43 ppm (1σ), respectively) from the domain proximal to our APT specimens in our calculations. For the untreated grain, mean U is 233 ± 48 (1σ) and Th is 116 ± 30 ppm (1σ).

DISCUSSION

Atom probe and TEM analyses of experimentally heated zircon reveal two types of clusters, neither of which are observed in APT specimens from the untreated zircon. Although the cluster types differ with respect to composition, morphology and size, the Pb isotopic ratio extracted from both types of clusters is the same, within the uncertainty of our measurements. The contemporaneous formation of these cluster types merits discussion regarding the timing and mechanisms of trace element segregation in zircon.

The timing of Pb cluster formation

To determine the timing of Pb clustering, we first consider the geological context. After initial assembly and stabilization, the Kaapvaal Craton was affected by several accretionary tectonic events, the most significant of which was the Namaqua-Natal orogenic event, which spanned from 1.2 to 1.0 Ga (Baughman and Flowers 2020). If the clusters formed in response to a geologic event, such as the assembly of the Kaapvaal Craton ~3.0 Ga or the Namaqua-Natal orogenesis and the emplacement of large igneous bodies ~1.2 Ga, the ²⁰⁷Pb/²⁰⁶Pb of the clusters would have effectively ceased to evolve from the time of the geologic event because the clusters contain no elevated U (Valley et al. 2015; Peterman et al. 2016, 2019; Lyon et al. 2019). At U concentrations of 249 ppm, we calculate a U density of ~2 atoms U per 500 nm³ volume (the approximate size of the clusters). Given the half-lives of the ²³⁸U and ²³⁵U and assuming the maximum interval over which U within the clusters could have decayed (3.1 Ga), these concentrations would correspond to a maximum of 2 atoms of ²⁰⁶Pb and 1 atom of ²⁰⁷Pb that could have been produced from U located within the clusters. These uncertainties are equivalent to our counting statistics, so the potential contribution of Pb atoms from U trapped in the clusters is negligible.

Assuming no common Pb at the time of zircon growth and a crystallization age of 3.13 Ga, the modeled cluster Pb ratios are 0.569 or 0.320 for 3.0 and 1.2 Ga events, respectively. However, the measured $^{207}\text{Pb}/^{206}\text{Pb}$ ratios from the clusters of 0.264 ± 0.025 are consistent with modern-day Pb isotopic ratios from an undisturbed 3.27 ± 0.15 Ga (1σ) zircon; this date is broadly consistent with dates measured from a nearby granitoid $[3.13 \pm 0.06$ Ga (1σ) from the air-abraded grains; Schoene and Bowring 2007]. Therefore, we conclude that the clustering of Pb, and the spatially associated trace elements, was produced by the laboratory-induced heating of the grain for 24 h at 1450 °C, and there has been no nanoscale disruption to the U-Pb isotopic system by geologic processes since the original crystallization. These interpretations are further corroborated by the absence of nanoscale features in the untreated zircon from the same sample. Notably, the absence of clusters in

this untreated zircon, as well as results from other zircon specimens (e.g., Exertier et al. 2018; Saxey et al. 2018; Peterman et al. 2019; Reddy et al. 2020) precludes sample preparation as a cause of cluster formation.

Mechanisms of cluster formation

Previous work on nanoscale trace element clustering in zircon and monazite suggests a range of possible mechanisms for trace element segregation, including the production of metallic Pb nanospheres via phase separation in response to UHT metamorphism (Kusiak et al. 2015; Whitehouse et al. 2017), exsolution of distinct mineral inclusions during secondary processes (Fougerouse et al. 2018; Seydoux-Guillaume et al. 2019), spinodal decomposition of zircon-xenotime solid solution (Peterman et al. 2019), and the accumulation of trace elements in either amorphous domains (Valley et al. 2014, 2015) or dislocation loops (Peterman et al. 2016, 2019) in response to diffusion. Compositional analysis of the experimentally induced clusters indicates that the clusters are trace-element-enriched zircon, not a compositionally distinct phase (Fig. 3). Therefore, despite the high T of our experimental heating conditions, there is no evidence for phase separation to produce metallic Pb nanospheres (cf. Kusiak et al. 2015; Whitehouse et al. 2017) or the exsolution of distinct mineral inclusions (Fougerouse et al. 2018; Seydoux-Guillaume et al. 2019). Furthermore, Y and P do not co-vary (Fig. 3), which rejects the possibility that these trace element clusters were produced by spinodal decomposition of zircon-xenotime (Peterman et al. 2019).

The other postulated mechanism for trace element clustering is segregation to defects. Because of the low diffusivity of Pb in crystalline zircon (e.g., Cherniak et al. 1991; Cherniak 2010), diffusive transport of Pb (and other trace elements) of more than a few nanometers under most geologic conditions is greatly facilitated by significant accumulation of radiation damage (Geisler et al. 2001; Ewing et al. 2003; Cherniak 2010). Using the measured concentrations for U and Th (249 and 163 ppm, respectively) and the known age of crystallization, we calculate an integrated α -dose of 4.4×10^{18} α/g , which is near the second percolation point for zircon (Murakami et al. 1991; Salje et al. 1999; Ewing et al. 2003; Pidgeon 2014). By 1.2 Ga (the timing of the Namaqua-Natal orogenic event), the zircon would have accumulated most of its radiation damage (3.2 \times 10¹⁸ α /g), but large-scale structural recovery is not expected to have occurred at temperatures of 200 °C (Meldrum et al. 1998; Garver et al. 1999; Geisler et al. 2001; Nasdala et al. 2001, 2004; Ginster et al. 2019), which is the peak temperature of the Namaqua-Natal orogenic event (Baughman and Flowers 2020).

In sum, these data indicate that the analyzed zircon had accumulated significant radiation damage prior to our experiments, despite a low-*T* thermal event at ~1.2 Ga. Pb was mobilized during laboratory heating, consistent with the high rates of Pb diffusion at our experimental conditions, particularly in radiation-damaged zircon (Cherniak 2010), and confirmed by the Pb isotopic ratio extracted from the clusters. These results also show that a single, high-*T*, short-duration thermal event can lead to the formation of morphologically different clusters at the nanoscale, indicating that morphology alone cannot be used to infer that multiple cluster populations mean multiple thermal events.

Crystallographic controls on trace element segregation

The clusters observed in APT are preferentially located in {100} and {001} and exhibit a loop-like structure (Fig. 2). The TEM data show that these loop-like structures have Moiré fringes associated with loop-parallel defects (Fig. 5) and high concentrations of particular trace elements (Figs. 2, 5d, and 5e). We, therefore, interpret these features as trace-element-enriched dislocation loops. In contrast with the well-known annealing of fission tracks and other point defects at relatively low temperatures (~200 °C; e.g., Garver et al. 1999), the production of dislocation loops requires significantly higher temperatures. Dislocation loops measuring 10–100 nm have been shown to form in radiation-damaged zircon in response to 24 h heating experiments at 1250 and 1450 °C (Bursill and McLaren 1966), which is consistent with our experiments.

We also observe a crystallographic control on the size and composition of the dislocation loops. Our TEM data show that the loops lie in {100} and {001}, with the loop edges aligned with <100>, <001>, and <101>. The largest loops are preferentially located in {100} planes that are parallel to the z-axis of the atom probe specimen. Notably, higher concentrations of Mg and Al are found parallel to <001> within these larger loops (Figs. 2c and 3). Smaller loops found in {100} and {001} contain the same trace elements, but Mg, Al, and Y are homogeneously distributed and do not appear to define loop-like features (Fig. 2d). Mg and Al are commonly interstitial in zircon (Hoskin and Ireland 2000; Hoskin and Schaltegger 2003) and more mobile than trace elements incorporated into the zircon lattice, as demonstrated by anomalously high concentrations of Mg and Al associated with Cottrell atmospheres around dislocations (Reddy et al. 2016, 2020). As dislocations moved through the crystal, we suggest that mobile, interstitial trace elements segregated to lower energy sites associated with dislocation loops, which were being produced simultaneously. The distribution of Mg+Al in {100} planes is consistent with slip along the {100} previously identified in zircon (Reddy et al. 2007). Although our results differ from earlier work by Bursill and McLaren (1966), which suggested that dislocation loops lie in {101} planes with Burgers vectors parallel to <101>, our findings are consistent with energetically favorable slip systems in zircon (Reddy et al. 2007; Timms et al. 2012), yielding a self-consistent result for the formation, composition, and distribution of dislocation loops within the zircon.

Comparison with naturally formed dislocation loops

The dislocation loops observed in this study are similar in size and morphology to those observed by our prior analyses of radiation-damaged zircon from the Rhodope Metamorphic Complex, located in eastern Greece (Peterman et al. 2016). We also observe similarities in the distribution of elements within the loops. As with the Kaapvaal zircon, Pb in the Rhodope zircon is concentrated into two bands, and the 3D reconstructions of the loops (cf. Online Materials¹; Peterman et al. 2016) show that the loops themselves are flattened and inclined with respect to the z-axis of the atom probe specimen. These data are consistent with some crystallographic control on the distribution of trace elements within the loops. Although we lack the precise orientation of the atom probe specimen to be able to assess if the Pb-rich loops are similarly located within {100}, results from EBSD analysis (Peterman et al. 2016) suggest that this is probable and

is consistent with the results of this study.

We observe two key differences between the dislocation loops in Rhodope and Kaapvaal zircon grains. First, the Rhodope loops contain high concentrations of Y+Pb, whereas the Kaapvaal loops contain high concentrations of Y, Pb, Mg, Al, and Yb. However, in both cases, the trace elements found at high concentrations are interstitial and relatively incompatible in zircon. We suspect that differences in composition among dislocation loops are related to the original composition of the zircon, but the data set is not yet large enough to directly test this hypothesis.

A second key difference is that a typical atom probe specimen from the core of the Rhodope zircon contains fewer than five dislocation loops, whereas the experimentally heated Kaapvaal grain contains hundreds of loops in each APT specimen. Differences in dislocation loop density may be related to: the radiation dose at the time of heating, the P-T conditions under which the loops formed, or the rate of heating and/or structural recovery and annealing. We observe fewer dislocation loops in the Rhodope zircon than the Kaapvaal grain, despite the significantly higher radiation dose at the time of cluster formation $(8.8 \times 10^{18} \text{ a/g} \text{ for Rhodope vs. } 4.4$ \times 10¹⁸ α /g for Kaapvaal), indicating that dislocation loop density is not directly correlated with radiation dose. Instead, we suggest that the difference in dislocation loop density between the Rhodope and Kaapvaal grains is a function of the amount of recrystallization that occurred prior to dislocation loop formation, which is a function of the P-T history. Geologic storage at 700 °C for 370 Myr can result in complete structural recovery (Geisler et al. 2001), but storage at these conditions for such an extended interval is unlikely. At lower temperatures, the zircon may partially recover, but we would not expect to observe dislocation loops. In contrast, relatively short duration geologic events (>100 kya) at elevated temperature (>900 °C) would likely mobilize Pb (and other incompatible trace elements) while structural recovery is ongoing, thereby simultaneously producing dislocation loops. These findings suggest that the production and density of dislocation loops may depend on the rate, duration, and absolute temperature of geologic heating.

To explore the geologic significance of differences in cluster density, we sought additional context by comparing the P-T histories of three additional radiation-damaged zircon grains that have been analyzed by APT, some of which have clusters that are similar in composition and size to those observed in the Kaapvaal and Rhodope grains (Table 1). Two examples come from the Jack Hills (Western Australia) and a third was sampled from the Grouse Creek Mountains (Utah, U.S.A.). The Jack Hills zircon grains are 4.4 and 4.0 Ga; the 4.4 Ga grain has a 3.4 Ga rim and the APT specimen contains hundreds of Y+Pb clusters (Valley et al. 2015). In contrast, the 4.0 Ga Jack Hills grain does not have a younger rim and the APT specimen lacks any clusters (Valley et al. 2015). The 2.5 Ga Grouse Creek grain has a young igneous rim attributed to a geologic event at 29 Ma and the APT specimen from this sample contains a similar density of clusters to the 4.4 Ga Jack Hills specimen (Valley et al. 2015). For comparison, the Kaapvaal specimens contain hundreds of loops, and there is no geological evidence of moderate- to high-T annealing of the grain prior to our laboratory experiments. The Rhodope zircon was metamorphosed during subduction to UHP conditions along a relatively cold thermal gradient (Krenn et al. 2010); the younger rim formed during upper amphibolite to granulite facies metamorphism following the UHP

TABLE 1. Attributes of zircons analyzed by APT

	Rhodope ^a	Kaapvaal	Jack Hills 4.4 ^b	Jack Hills 4.0 ^b	Grouse Creek ^b
Crystallization age	2144 ± 33 Ma	3268 ± 150 Ma	4374 ± 6 Ma	4007 ± 22 Ma	2542 ± 5 Ma
Cluster density	Low	High	High	None	High
% concordance of zircon core	66	n.d.	100	97	97
Rim age	180–150 Ma	n/a	3400 Ma	n/a	29 Ma
α/g at time of rim formation	8.1×10^{18}	4.4×10^{18}	Estimated at 1.83×10^{18c}	n/a	8.05×10^{18}
Origin and dT/dt of second event	Metamorphic; low dT/dt	Laboratory; high dT/dt	Igneous; high dT/dt	n/a	Igneous; high dT/dt

Notes: n.d. = not determined; n/a = not applicable. Peterman et al. (2016). Valley et al. (2015). Estimated based on approximate U and Th concentrations (145 and 100 ppm, respectively) and ages of geologic events reported in Valley et al. (2015).

event (Peterman et al. 2016, 2019). APT specimens from this grain contain a few clusters enriched in trace elements.

Among the zircon specimens with high cluster densities, the Kaapvaal grain was subjected to a steep dT/dt (400 °C/h), and the rim-forming events for the 4.4 Ga Jack Hills and 2.5 Ga Grouse were igneous and thus also high dT/dt, with no Pb loss. In contrast, dT/dt for the Rhodope grain was more gradual, and Pb loss was interpreted to have occurred early in the prograde history (Peterman et al. 2016, 2019) because Pb is relatively mobile in radiationdamaged zircon (Cherniak 2010). As the temperature increased with progressive metamorphism, structural recovery began, which resulted in a more crystalline zircon and fewer defects available to produce dislocation loops. As a direct consequence, the zircon contains fewer dislocation loops, despite the high-radiation dose. Migrating Pb, enabled by increasing temperatures, was trapped in dislocation loops, thereby yielding a 207Pb/206Pb model age consistent with Pb mobility at the time of dislocation loop formation. These results suggest that the formation of dislocation loops requires both accumulated radiation damage and high(er) temperature geologic events. Importantly, dT/dt appears to play a significant role in both the density of clusters and amount of Pb loss.

If the clusters in the 4.4 Ga Jack Hills grain are produced by the same processes, our model suggests that they formed during the high-T geologic event that produced the 3.4 Ga rims; the modeled Pb ages of the clusters and the observation of a preferred crystallographic orientation for the clusters [parallel to (100) and (010); Valley et al. 2015] are consistent with this interpretation. Similarly, the Grouse Creek grain is a xenocryst with a 29 Ma igneous rim; these igneous processes could have thermally induced the formation of dislocation loops, which trapped migrating Pb.

IMPLICATIONS

The segregation of incompatible trace elements to clusters has been reported in natural samples of metamorphically heated zircon (Valley et al. 2014, 2015; Peterman et al. 2016, 2019). However, the observation that short interval, high-*T* heating of zircon (e.g., 1450 °C, 24 h) can produce large numbers of similar segregation features suggests that the presence of decorated dislocation loops may be useful in identifying short duration, high-*T* geologic events. Such events may include thermal spikes associated with melt sheets formed during impact cratering (Arcuri et al. 2020) or the entrapment of zircon xenocrysts in volcanic rocks.

In natural examples of trace element segregation to dislocation loops, the data indicate that these features form during the prograde evolution of the metamorphosed zircon (Peterman et al. 2016) and are therefore not destroyed at peak temperatures of >800 °C over several million years. Once formed, trace element segregations within dislocation loops are likely to serve as a durable reservoir for trace element entrapment in zircon. This has potential implications

for understanding diffusion in zircon because diffusion out of these segregations will have a fundamentally different activation energy than typical volume diffusion. In addition, the segregations may continue to act as a local sink for trace elements diffusing through the zircon lattice. In these cases, the behavior of trace elements within segregations may become decoupled from those that are not segregated, for example, Pb and Ti, respectively, which may have implications for deriving *T-t* histories from zircon at the nanoscale.

The entrapment of particular trace elements in nanoscale defects has potential minerals engineering applications. Zircon has been considered as a potential repository for nuclear waste materials (e.g., Ewing 1999) because it is considered to be physically and chemically stable over geological timescales. The experimental data presented here indicate that nanoscale segregations of entrapped trace elements can be engineered under laboratory conditions over short timescales (hours to days), even in robust minerals such as zircon. These segregations provide an additional level of geochemical isolation from the environment and may prove useful in the storage of noxious materials, such as nuclear waste.

ACKNOWLEDGMENTS

The authors thank Callum Hetherington for editorial handling and Lee White and two anonymous reviewers for providing constructive comments. Peterman thanks Jaclyn Baughman (Humboldt State University) for providing the zircon separate, Jonathan Stebbins (Stanford) for the use of his high-temperature furnaces, Marty Grove (Stanford) for supporting Peterman's Blaustein appointment at Stanford, and the Blaustein Visiting Researcher fund at Stanford University.

FUNDING

This work was supported in part by Bowdoin College Research Funds. The SEMs at Bowdoin College and Curtin University were supported by NSF MRI-1530963 to E. Peterman and R. Beane and ARC LE 190100176 to S. Reddy and Z. Quadir, respectively. The development of the Geoscience Atom Probe Facility was supported by the Science and Industry Endowment Fund (SIEF) through Grant SIEF RII3-01 to S. Reddy. D. Fougerouse is supported by the Australian Research Council (ARC DE190101307).

REFERENCES CITED

Allaz, J.M., Williams, M.L., Jercinovic, M.J., Goemann, K., and Donovan, J. (2019) Multipoint background analysis: Gaining precision and accuracy in microprobe trace element analysis. Microscopy and Microanalysis, 25, 30–46.

Arcuri, G., Moser, D., Reinhard, D., Langeleir, B., and Larson, D. (2020) Impact-triggered nanoscale Pb clustering and Pb loss domains in Archean zircon. Contributions to Mineralogy and Petrology, 175, 59.

Baughman, J.S., and Flowers, R.M. (2020) Mesoproterozoic burial of the Kaapvaal craton, southern Africa during Rodinia supercontinent assembly from (U-Th)/He thermochronology. Earth and Planetary Science Letters, 531, 115930.

Blum, T.B., Darling, J.R., Kelly, T.F., Larson, D.J., Moser, D.E., Perez-Huerta, A., Prosa, T.J., Reddy, S.M., Reinhard, D.A., Saxey, D.W., Ulfig, R., and Valley, J.W. (2018) Best practices for reporting atom probe analysis of geological materials. In D.E. Moser, F. Corfu, J.R. Darling, S.M. Reddy, and K. Tait, Eds., Microstructural Geochronology: Planetary Records Down to Atom Scale, 369–373. American Geophysical Union.

Bursill, L.A., and McLaren, A.C. (1966) Transmission electron microscope study of natural radiation damage in zircon (ZrSiO₄). Physica status solidi (b), 13, 331–343.Cherniak, D.J. (2010) Diffusion in accessory minerals: Zircon, titanite, apatite, monazite and xenotime. Reviews in Mineralogy and Geochemistry, 72, 827–869.

Cherniak, D.J., and Watson, E.B. (2003) Diffusion in zircon. In J.M. Hanchar and P.W.O.

- Hoskin, Eds., Zircon. Reviews in Mineralogy and Geochemistry, 53, 113-143.
- Cherniak, D.J., Lanford, W.A., and Ryerson, F.J. (1991) Lead diffusion in apatite and zircon using ion implantation and Rutherford backscattering techniques. Geochimica et Cosmochimica Acta, 55, 1663–1673.
- de Wit, M.J., Roering, C., Hart, R.J., Armstrong, R.A., de Ronde, C.E.J., Green, R.W.E., Tredoux, M., Peberdy, E., and Hart, R.A. (1992) Formation of an Archean continent. Nature, 357, 553–562.
- Ewing, R.C. (1999) Nuclear waste forms for actinides. Proceedings of the National Academy of Sciences, 96, 3432–3439.
- Ewing, R.C., Meldrum, A., Wang, L., Weber, W.J., and Corrales, L.R. (2003) Radiation effects in zircon. In J.M. Hanchar and P.W.O. Hoskin, Eds., Zircon. Reviews in Mineralogy and Geochemistry, 53, 387–425.
- Exertier, F., La Fontaine, A., Corcoran, C., Piazolo, S., Belousova, E., Peng, A., Gault, B., Saxey, D.W., Fougerouse, D., Reddy, S.M., and others (2018) Atom probe tomography analysis of the reference zircon GJ-1: An interlaboratory study. Chemical Geology, 495, 27–35.
- Fougerouse, D., Reddy, S.M., Saxey, D.W., Rickard, W.D.A., van Riessen, A., and Micklethwaite, S. (2016) Nanoscale gold clusters in arsenopyrite controlled by growth rate not concentration: evidence from atom probe microscopy. American Mineralogist, 101, 1916–1919.
- Fougerouse, D., Reddy, S.M., Saxey, D.W., Erickson, T.M., Kirkland, C.L., Rickard, W.D.A., Seydoux-Guillaume, A.M., Clark, C., and Buick, I.S. (2018) Nanoscale distribution of Pb in monazite revealed by atom probe microscopy. Chemical Geology, 479, 251–258.
- Garver, J.I., Brandon, M.T., Roden-Tice, M.K., and Kamp, P.J.J. (1999) Exhumation history of orogenic highlands determined by detrital fission-track thermochronology. In A.J. Fleet, R.E. Holdsworth, A.C. Morton, and M.S. Stoker, Eds., Exhumation Processes: Normal faulting, ductile flow, 154, 283–304. Geological Society of London Special Publications
- Ge, R., Wilde, S.A., Nemchin, A.A., Whitehouse, M.J., Bellucci, J.J., Erickson, T.M., Frew, A., and Thern, E.R. (2018) A 4463 Ma apparent zircon age from the Jack Hills (Western Australia) resulting from ancient Pb mobilization. Geology, 46, 303–306.
- Geisler, T. (2002) Isothermal annealing of partially metamict zircon: Evidence for a three-stage recovery process. Physics and Chemistry of Minerals, 29, 420–429.
- Geisler, T., Pidgeon, R.T., van Bronswijk, W., and Pleysier, R. (2001) Kinetics of thermal recovery and recrystallization of partially metamict zircon: A Raman spectroscopic study. European Journal of Mineralogy, 13, 1163–1176.
- Geisler, T., Schaltegger, U., and Tomaschek, F. (2007) Re-equilibration of zircon in aqueous fluids and melts. Elements, 3, 43–50.
- Ginster, U., Reiners, P.W., Nasdala, L., and Chanmuang, N.C. (2019) Annealing kinetics of radiation damage in zircon. Geochimica et Cosmochimica Acta. 249, 225–246.
- Harley, S.L., Kelly, N.M., and Moller, A. (2007) Zircon behaviour and the thermal histories of mountain chains. Elements, 3, 25–30.
- Hazen, R.M., and Finger, L.W. (1979) Crystal structure and compressibility of zircon at high pressure. American Mineralogist, 64, 196–201.
- Hellman, O.C., Vandenbroucke, J.A., Rüsing, J., Isheim, D., and Seidman, D.N. (2000) Analysis of three-dimensional atom-probe data by the proximity histogram. Microscopy and Microanalysis, 6, 437–444.
- Hoskin, P.W.O., and Ireland, T.R. (2000) Rare earth element chemistry of zircon and its use as a provenance indicator. Geology, 28, 627–630.
- Hoskin, P.W.O., and Schaltegger, U. (2003) The composition of zircon and igneous and metamorphic petrogenesis. In J.M. Hanchar and P.W.O. Hoskin, Eds., Zircon. Reviews in Mineralogy and Geochemistry, 53, 27–62.
- Krenn, K., Bauer, C., Proyer, A., Klötzli, U., and Hoinkes, G. (2010) Tectonometamorphic evolution of the Rhodope orogen. Tectonics, 29, TC4001. doi: 10.1029/2009TC002513.
- Kusiak, M.A., Whitehouse, M.J., Wilde, S.A., Nemchin, A.A., and Clark, C. (2013) Mobilization of radiogenic Pb in zircon revealed by ion imaging: Implications for early Earth geochronology. Geology, 41, 291–294.
- Kusiak, M.A., Dunkley, D.J., Wirth, R., Whitehouse, M.J., Wilde, S.A., and Marquardt, K. (2015) Metallic lead nanospheres discovered in ancient zircons. Proceedings of the National Academy of Sciences, 112, 4958–4963.
- Layer, P.W., Kroner, A., and York, D. (1992) Pre-3000 Ma thermal history of the Archean Kaap valley pluton. Geology, 20, 717–720.
- Lyon, I.C., Kusiak, M.A., Wirth, R., Whitehouse, M.J., Dunkley, D.J., Wilde, S.A., Schaunlöffel, D., Malherbe, J., and Moore, K.L. (2019) Pb nanospheres in ancient zircon yield model ages for zircon formation and Pb mobilization. Nature, 9, 13702. https://doi.org/10.1038/s41598-019-49882-8.
- Meldrum, A., Boatner, L.A., Weber, W.J., and Ewing, R.C. (1998) Radiation damage in zircon and monazite. Geochimica et Cosmochimica Acta, 62, 2509–2520.
- Montalvo, S.D., Reddy, S.M., Saxey, D.W., Rickard, W.D.A., Fougerouse, D., Quadir, Z., and Johnson, T.E. (2019) Nanoscale constraints on the shock-induced transformation of zircon to reidite. Chemical Geology, 507, 85–95.
- Murakami, T., Chakoumakos, B.C., Ewing, R.C., Lumpkin, G.R., and Weber, W.J. (1991) Alpha-decay event damage in zircon. American Mineralogist, 76, 1510–1532.
- Nasdala, L., Wenzel, M., Vavr, G., Irmer, G., Wenzel, T., and Kober, B. (2001) Metamictization of natural zircon: accumulation versus thermal annealing of radioactivityinduced damage. Contributions to Mineralogy and Petrology, 141, 125–144.
- Nasdala, L., Lengauer, C.L., Hanchar, J.M., Kronz, A., Wirth, R., Blanc, P., Kennedy,

- A.K., and Seydoux-Guillaume, A.-M. (2002) Annealing radiation damage and the recovery of cathodoluminescence. Chemical Geology, 191, 121–140.
- Nasdala, L., Reiners, P.W., Garver, J.I., Kennedy, A.K., Stern, R.A., Balan, E., and Wirth, R. (2004) Incomplete retention of radiation damage in zircon from Sri Lanka. American Mineralogist, 89, 219–231.
- Peterman, E.M., Reddy, S.M., Saxey, D.W., Snoeyenbos, D.R., Rickard, W.D.A., Fougerouse, D., and Kylander-Clark, A.R.C. (2016) Nanogeochronology of discordant zircon measured by atom probe microscopy of Pb-enriched dislocation loops. Science Advances, 2, e:1601218.
- Peterman, E.M., Reddy, S.M., Saxey, D.W., Fougerouse, D., Snoeyenbos, D.R., and, and Rickard, W.D.A. (2019) Nanoscale processes of trace element mobility in metamorphosed zircon. Contributions to Mineralogy and Petrology, 174, 92.
- Piazolo, S., La Fontaine, A., Trimby, P., Harley, S., Yang, L., Armstrong, R., and Cairney, J.M. (2016) Deformation-induced trace element redistribution in zircon revealed using atom probe tomography. Nature Communications, 7, 10490.
- Pidgeon, R.T. (2014) Zircon radiation damage ages. Chemical Geology, 367, 13-22.
- Pouchou, J.-L., and Pichoir, F. (1984) A new model for quantitative X-ray microanalysis. 1. Application to the analysis of homogeneous samples. La Recherche Aerospatiale, 3, 167–192.
- Reddy, S.M., Timms, N.E., Pantleon, W., and Trimby, P. (2007) Quantitative characterization of plastic deformation of zircon and geologic implications. Contributions to Mineralogy and Petrology, 153, 625–645.
- Reddy, S.M., van Riessen, A., Saxey, D.W., Johnson, T.E., Rickard, W.D.A., Fougerouse, D., Fischer, S., Prosa, T.J., Rice, K.P., Reinhard, D.A., Chen, Y., and Olson, D. (2016) Mechanisms of deformation-induced trace element migration in zircon resolved by atom probe and correlative microscopy. Geochimica et Cosmochimica Acta, 195, 158–170.
- Reddy, S.M., Saxey, D.W., Rickard, W.D.A., Fougerouse, D., Montalvo, S.D., Verberne, R., and Riessen, A. (2020) Atom probe tomography: Development and application to the geosciences. Geostandards and Geoanalytical Research, 44, 5–50.
- Rickard, W.D.A., Reddy, S.M., Saxey, D.W., Fougerouse, D., Timms, N.E., Daly, L., Peterman, E., Cavosie, A.J., and Jourdan, F. (2020) Novel applications of FIB-SEM-based ToF-SIMS in atom probe tomography workflows. Microscopy and Microanalysis, 26, 750–757.
- Rubatto, D. (2002) Zircon trace element geochemistry: Partitioning with garnet and the link between U–Pb ages and metamorphism. Chemical Geology, 184, 123–138.
- Salje, E.K.H., Chrosch, J., and Ewing, R.C. (1999) Is "metamictization" of zircon a phase transition? American Mineralogist, 84, 1107–1116.
- Saxey, D.W., Reddy, S.M., Fougerouse, D., and Rickard, W.D.A. (2018) The optimization of zircon analyses by laser-assisted atom probe microscopy: Insights from the 91500 zircon standard. In D.E. Moser, F. Corfu, J.R. Darling, S.M. Reddy, and K. Tait, Eds., Microstructural Geochronology: Planetary records down to atom scale, p. 293–313. Wiley.
- Saxey, D., Fougerouse, D., Rickard, W., and Reddy, S. (2019) Spatial reconstruction of atom probe data from zircon. Microscopy and Microanalysis, 25, 2536–2537.
- Schoene, B. (2014) U-Th-Pb geochronology. In R. Rudnick, Ed., Treatise on Geochemistry, 4.10, 341–378.
- Schoene, B., and Bowring, S.A. (2007) Determining accurate temperature–time paths from U-Pb thermochronology: An example from the Kaapvaal craton, southern Africa. Geochimica et Cosmochimica Acta, 71, 165–185.
- Seydoux-Guillaume, A.-M., Fougerouse, D., Laurent, A., Gardés, E., Reddy, S., and Saxey, D. (2019) Nanoscale resetting of the Th/Pb system in an isotopically-closed monazite grain: A combined atom probe and transmission electron microscopy study. Geoscience Frontiers, 10, 65–76.
- Timms, N.E., Reddy, S.M., Healy, D., Nemchin, A.A., Grange, M.L., Pidgeon, R.T., and Hart, R. (2012) Resolution of impact-related microstructures in lunar zircon: A shock-deformation mechanism map. Meteoritics & Planetary Science, 47, 120–141.
- Valley, J.W., Cavosie, A.J., Ushikubo, T., Reinhard, D.A., Lawrence, D.F., Larson, D.J., Clifton, P.H., Kelly, T.F., Wilde, S.A., Moser, D.E., and Spicuzza, M.J. (2014) Hadean age for a post-magma-ocean zircon confirmed by atom-probe tomography. Nature Geoscience, 7, 219–223.
- Valley, J.W., Reinhard, D.A., Cavosie, A.J., Ushikubo, T., Lawrence, D.F., Larson, D.J., Kelly, T.F., Snoeyenbos, D.R., and Strickland, A. (2015) Nano-and microgeochronology in Hadean and Archean zircons by atom-probe tomography and SIMS: New tools for old minerals. American Mineralogist, 100, 1355–1377.
- Whitehouse, M.J., Kusiak, M.A., Wirth, R., and Ravindra Kumar, G.R. (2017) Metallic Pb nanospheres in ultra-high temperature metamorphosed zircon from southern India. Mineralogy and Petrology, 111, 467–474.

Manuscript received June 5, 2020 Manuscript accepted December 24, 2020 Manuscript handled by Callum Hetherington

Endnote:

¹Deposit item AM-21-127654, Online Materials. Deposit items are free to all readers and found on the MSA website, via the specific issue's Table of Contents (go to http://www.minsocam.org/MSA/AmMin/TOC/2021/Dec2021_data/Dec2021_data.html).